Thermomechanical Behavior of the Solidifying Strand in Secondary Cooling

Nathan M. Seymour[1], Brian G. Thomas[1,2]

[1]University of Illinois Urbana-Champaign
Department of Mechanical Science and Engineering
1206 West Green Street, Urbana, IL, USA, 61801
Phone: +1 (217) 333-6919
Email: nseymou2@illinois.edu, bgthomas@illinois.edu

[2]Colorado School of Mines
Department of Mechanical Engineering
1500 Illinois Street, Golden, Colorado 80401, USA
Phone: 303-273-3309
E-mail: bgthomas@mines.edu

Keywords: continuous casting, solidification, secondary cooling, transverse cracks, fatigue

ABSTRACT

The thermo-mechanical behavior of the solidifying steel strand from meniscus to caster exit is explored in this work with a small-slice computational model based on CON1D[1] and ABAQUS[2], using specialized boundary conditions to simulate loading during mold and secondary cooling. Different compressive and tensile loading is observed at the inside- and outside-radii due to bending and unbending. Locations near the strand surface experience two complete stress-strain cycles between every roll pair in secondary cooling due to surface quenching from roll contact and water sprays. Stress-strain cycling results from surface quenching during secondary cooling are shown. The complex stress and inelastic strain histories experienced near the strand surface contribute to the formation of transverse cracks, and provide insight for future work.

INTRODUCTION

Transverse crack formation is a serious issue in continuous casting of steel, and the correlation between particular microstructural features and crack formation has been studied by researchers[3,4]. The presence of abnormally large austenite grains, grain boundary ferrite and grain boundary precipitates all contribute to the formation of intergranular transverse cracks. Secondary cooling methods that avoid the formation of grain boundary ferrite and grain boundary precipitates have been shown to decrease the formation of transverse cracks[5].

To study the crack susceptibility of specific steel grades, monotonic tensile tests at elevated temperatures have been used to quantify the steel ductility based on the reduction-in-area at failure[6,7]. These crack susceptibility tests have found qualitative correlation between a steel's reduction-in-area at failure and transverse crack susceptibility. However, the testing conditions of previous experimental steel ductility tests differ significantly from the complex thermo-mechanical loading conditions experienced by different locations in the steel strand in the real continuous caster. The microstructural features that accompany transverse cracks and the qualitative ductility of steel grades has received significant study, but quantitative information about the thermo-mechanical history experienced by the steel strand during secondary cooling is needed.

Previous computational models have quantified the heat transfer in a continuous caster[1,8,9]. Stress models have been developed to investigate the effects of bulging, bending, and stresses in the mold[9-11]. Few previous models have simulated the thermo-mechanical behavior through the entire caster, however. To accurately model the mechanical behavior of the steel during the entire continuous casting process, calibrated constitutive equations for the inelastic behavior of the steel are required. Steel constitutive equations should incorporate both elastic-viscoplastic behavior and kinematic hardening. The latter is needed because the steel strand experiences cyclic loading during secondary cooling, and kinematic hardening will avoid excessive hardening or elastic shakedown if large inelastic strains are accumulated. Accurate and useful experimental testing requires subjecting the samples to the same thermo-mechanical loading histories experienced in the caster. Computational models are essential tools to quantify the real loading conditions. Towards this goal, the current work develops a computational model to quantify the thermo-mechanical behavior of a typical slab caster in order to help avoid transverse crack formation.

COMPUTATIONAL MODEL

The thermo-mechanical behavior of the solidifying steel strand from meniscus to caster exit is quantified with a one-way coupled thermal and mechanical finite-element model developed in ABAQUS 6.13.2[2]. This Lagrangian model analyzes a narrow slice extending from the inside-radius (IR) surface to the outside-radius (OR) surface at the wide face centerline. This model domain travels through the caster at the casting speed, as shown in Figure 1, and so the thermo-mechanical boundary conditions vary with time below the meniscus. This analysis technique makes the valid assumption that axial conduction is negligible relative to advected energy transfer, as the Péclet number of the process is very large[1]. Special mechanical constraints are imposed on this small moving domain to realistically represent bending and unbending. This simple and efficient model was applied to investigate the behavior of the steel strand in the mold and secondary cooling.

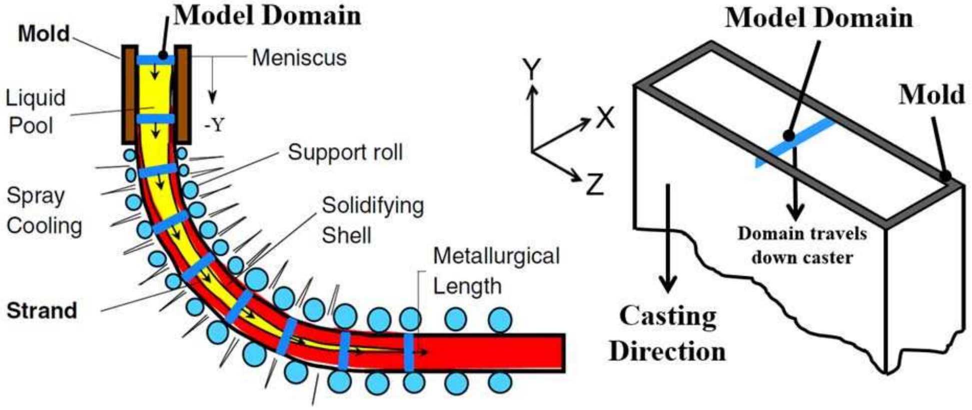

Figure 1. Location of the model domain in continuous slab-casting machine a) side view (*ccc.illinois.edu*); b) isometric view.

Governing Equations

A Lagrangian form of the two-dimensional (2-D) transient heat transfer equation is solved,

$$\rho\left(\frac{\partial H(T)}{\partial t}\right) = \nabla \cdot (k(T)\nabla T) \tag{1}$$

where ρ is the mass density, $H(T)$ is the temperature-dependent enthalpy, k is the isotropic thermal conductivity, and T is the temperature. Heat conduction in the transverse direction is zero due to symmetry.

The mechanical equilibrium equation is solved using two-dimensional generalized plane strain,

$$\nabla \cdot \boldsymbol{\sigma} = 0 \tag{2}$$

where $\boldsymbol{\sigma}$ is the stress tensor field. Body forces and related effects such as bulging due to gravity were neglected.

The strains are less than 0.025 m/m, so, the standard small-strain, linearized strain-displacement relation is appropriate:

$$\boldsymbol{\varepsilon} = \frac{1}{2}(\nabla \boldsymbol{u} + \nabla \boldsymbol{u}^{T}) \tag{3}$$

The total strain rate tensor is additively decomposed into three separate parts,

$$\dot{\boldsymbol{\varepsilon}} = \dot{\boldsymbol{\varepsilon}}_{\mathrm{el}} + \dot{\boldsymbol{\varepsilon}}_{\mathrm{th}} + \dot{\boldsymbol{\varepsilon}}_{\mathrm{ie}} \tag{4}$$

the elastic, thermal and inelastic strain rate tensors. The thermal strain tensor was calculated from:

$$\boldsymbol{\varepsilon}_{\mathrm{th}} = \alpha(T)\left(T - T_{ref}\right)\boldsymbol{I} \tag{5}$$

where $\alpha(T)$ is the isotropic temperature-dependent coefficient of thermal expansion, $\boldsymbol{I}$ is the identity tensor, and T_{ref} is the reference temperature, defined here as the solidus temperature.

The inelastic strain tensor is calculated using two different elasto-viscoplastic type constitutive equations depending on the phases present in the steel. The elasto-viscoplastic equation used to model the steel behavior is determined according to

$$\dot{\bar{\varepsilon}}_{\mathrm{ie}} = \begin{cases} f_\gamma(\%C, T, \bar{\varepsilon}_{ie}, \bar{\sigma}) \; if \; \gamma \geq \; 0.90 \\ f_\delta(\%C, T, \bar{\varepsilon}_{ie}, \bar{\sigma}) \; if \; \gamma < 0.90 \end{cases} \tag{6}$$

where f_γ and f_δ are the elasto-viscoplastic constitutive equations for austenite and delta-ferrite developed by Kozlowski[12] and Zhu[13], respectively, γ is the phase fraction of austenite present, $\%C$ is the weight percent carbon in the steel alloy, T is the temperature, $\bar{\sigma}$ is the effective stress, $\bar{\varepsilon}_{ie}$ is the effective inelastic strain, and $\dot{\bar{\varepsilon}}_{\mathrm{ie}}$ is the effective inelastic strain rate.

The stress response is calculated from the elastic strains using Hooke's law

$$\boldsymbol{\sigma} = \mathbb{C}(T) : \boldsymbol{\varepsilon}_{el} \tag{7}$$

where $\mathbb{C}(T)$ is the temperature-dependent fourth order isotropic elastic stiffness tensor.

Boundary Conditions

Mold heat flux and convective film coefficients for the strand surface were calculated using CON1D[1] for a generic, representative caster. CON1D calculates the mold heat flux by determining the thermal resistance of the gap between the mold cold face and strand surface, including important phenomena such as: contact resistances, air gaps, conduction through the liquid and solid slag, radiation through the mold flux, water scale buildup at the mold cold face, mold hot face coatings, and oscillation marks. Convective film coefficient values from CON1D were calculated using an equation of the form

$$h_{spray} = A \; c \; Q_w{}^n \; (1 - bT_0) \tag{8}$$

where h_{spray} is the film coefficient in $[kW/m^2K]$, Q_w is the water flow rate in $[L/m^2s]$, T_0 is the water spray temperature, and A, c, n, b are constants with values from Nozaki[14]. Because heat transfer in steel continuous casting has a large Peclet number, heat conduction in the casting direction is neglected by insulating the top and bottom surfaces of the model domain. Heat conduction in the transverse direction is zero due to symmetry. The thermal boundary conditions are assumed to be the same at the inner and outer radius, so thermal results are symmetric about the strand centerline. Figure 2 shows the mold heat transfer boundary conditions and a representative portion of the convective film boundary conditions.

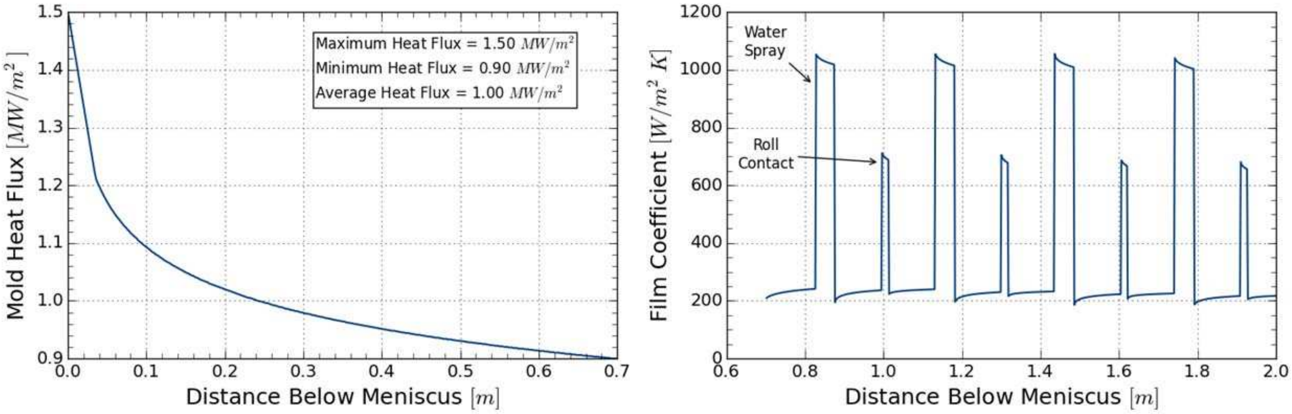

Figure 2. Thermal boundary conditions at the strand surface.

The peaks of the convective film coefficient correspond to the water spray and support roll contact zones in secondary cooling. The water spray zones are 50 mm wide, the roll contact zones are 18 mm wide, and the gaps between support roll contact and water spray are 118 mm wide. Natural convection and radiation control the energy removal from the strand during ambient cooling. A schematic illustrating the secondary cooling mechanisms is shown in Figure 3. Application of thermal boundary conditions at the strand surface in the mold and secondary cooling is performed using the ABAQUS user subroutines `DFLUX` and `FILM`, respectively.

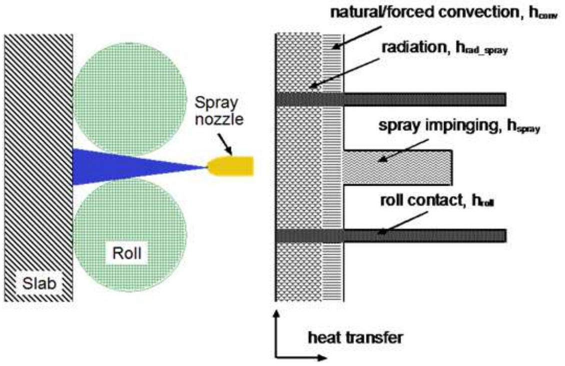

Figure 3. Schematic of secondary cooling mechanisms at the strand surface[1].

The mechanical response of the model is calculated based on temperature results input from the thermal model. The mechanical boundary conditions allow for free expansion and contraction of the caster cross-section's liquid core, and assume a machine taper of zero. Bending and unbending are imposed by controlling the slope of the top boundary of the model domain. The nodes on the top boundary of the model domain are constrained to remain in a straight line, thereby requiring that plane sections remain plane during bending of the steel strand. The slope m of this top boundary line is calculated as a function of the machine radius R and the initial thickness of the model domain in the casting direction d via:

$$m = tan\left(\frac{d}{R}\right) \tag{9}$$

Bending is applied by linearly ramping the slope of the top boundary line from zero to m during the time taken to pass between 3 roll contact points (twice the roll pitch) in the bending region. This is the shortest distance over which bending can be applied. Then, the slope m is maintained between the bending and unbending regions. Finally, the slope of the top boundary line is ramped linearly from m back to zero during the unbending region (again 3 roll contact points). Figure 4 illustrates how the slope of the top line of the model domain is controlled to simulate bending and unbending. Specifically, the following mechanical boundary conditions were applied: $u_x = 0$ at the IR and OR surfaces, $u_y = 0$ at the bottom surface, and $u_y = a(t) + m(t)x$ at the top surface. The latter was achieved with a slider multi-point constraint to force the top surface nodes into a line, and a linear constraint equation to control the line slope. The linear constraint equation used the displacement of a dummy node, u_{yD}, to control the top boundary slope by relating the y-displacements of the top right and top left nodes, u_{yNE} and u_{yNW} respectively. In this equation, W is the initial slab width, and u_{yD} is set to the slope m:

$$0 = -u_{yNE} + u_{yNW} - W\, u_{yD} \tag{8}$$

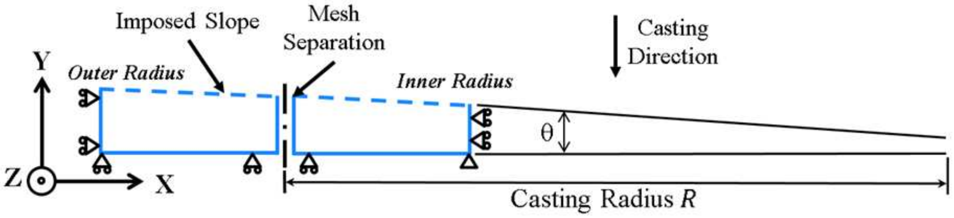

Figure 4. Bending and unbending boundary conditions on model domain.

A generalized plane strain condition is applied in the undiscretized Z-direction of the model domain. The ε_{zz} strain is allowed to vary linearly in the X-direction but is forced to remain constant in the Y-direction: $\varepsilon_{zz} = a(t) + b(t)x$ This allows the sides of the domain on the inner and outer radii to expand and contract in the Z-direction due to the Poisson effect during thermal cycling, bending and unbending. This boundary condition imposes the mechanical constraint that the narrow face must remain planar and orthogonal to the casting direction. Figure 5 shows the location of the generalized plane strain bounding plane[2] relative to the caster.

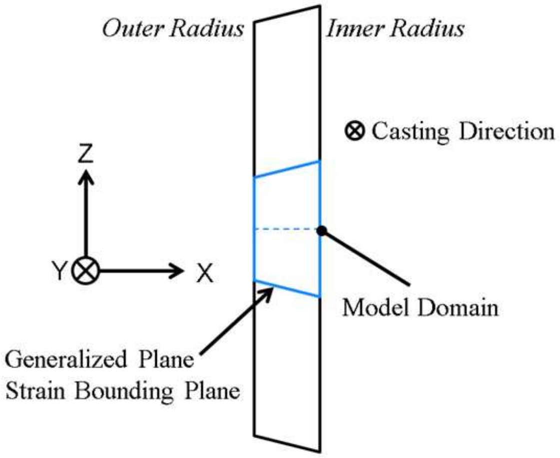

Figure 5. Generalized plane strain boundary conditions in the undiscretized direction.

The thermo-mechanical casting conditions used for this model are based on a previously developed CON1D model representation of the ArcelorMittal Burns Harbor caster[15]. The relevant thermal and mechanical parameters, including those used for bending and unbending, are given in Table I.

Table I. Thermo-mechanical casting conditions.

Modeling Parameter	**Value**	**Modeling Parameter**	**Value**
Mold Length [m]	0.690	Dwell Time [min]	28.2
Distance to Bender [m]	2.83	Casting Speed [m/min]	1.10
Bending Transition Length [m]	0.61	Initial Temperature [°C]	1550
Bending Arc Length [m]	23.56	Superheat [°C]	22
Unbending Transition Length [m]	0.61	$T_{liquidus}$ [°C]	1528
Caster Length [m]	31.0	$T_{solidus}$ [°C]	1508
Casting Radius [m]	15.0	T_{sink} for Spray Water [°C]	25
Slab Thickness [mm]	254.0		

Computational Details

In the thermal model, 8 node biquadratic quadrilateral diffusive heat transfer elements were used. In the mechanical model, 8 node biquadratic quadrilateral hybrid elements with linear pressure and generalized plane strain in the undiscretized direction were used. The ABAQUS codes for these two element types were DC2D8 and CPEG8H, respectively. The elements in the thermal and mechanical models are fully integrated with 3 × 3 Gauss-Legendre quadrature. The simplified model domain size was 260 mm by 1.5 mm, modeling a narrow cross-section extending completely through the centerline of the steel strand, which was 254mm thick at caster exit. The same mesh is used for both the thermal and mechanical models. A fine mesh of 0.5 mm x 0.5 mm elements was used for the first 30 mm below the strand surface. A coarser mesh of 1.0 mm x 0.5 mm elements was used for the inner 200 mm of the model domain. This model used 960 elements and 3,534 nodes. The thermal model ran in 23 min, and the mechanical model ran in 71 min. These times were achieved with ABAQUS 6.13.2 on one core of a 2.67 GHz Intel Xeon W3520 processor.

COMPUTATIONAL MODEL RESULTS

The thermal results from the ABAQUS model agree closely with those from CON1D, which has been partially validated with plant measurements in previous work[1,15]. The shell growth of the strand is shown in Figure 6, which also indicates the distances over which bending and unbending were applied. Bending and unbending were both applied over a distance of 0.61m, corresponding to a time of 33s for the casting speed of 1.10 m/min. The shell grew in thickness from 27 mm at the start of bending, to 31 mm thick at the end of bending. Similarly, during unbending, the shell grew from 114 mm to 116 mm in thickness. The shell thickness was calculated using the solidus temperature. Subsurface cracks could form at the solidification front at the OR during bending and at the IR during unbending. The metallurgical length was 28.0m.

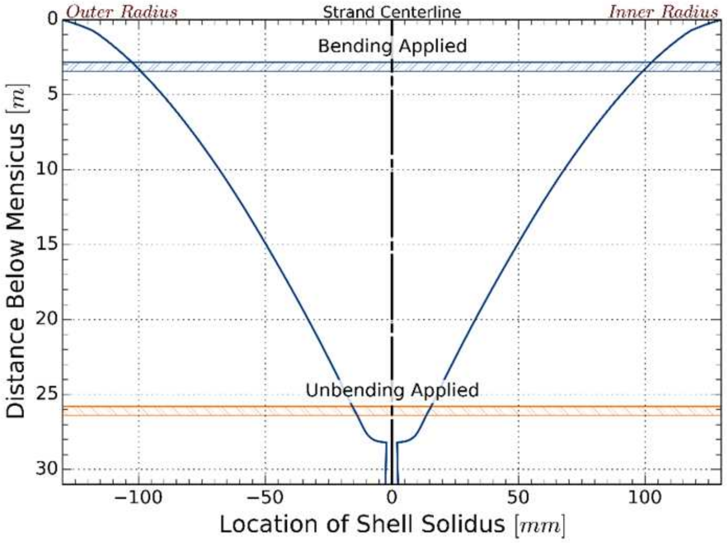

Figure 6. Shell thickness as a function of distance below meniscus.

The temperature and σ_{yy} profiles through the steel strand before bending was applied are shown in Figure 7. Non-uniform heat extraction during secondary cooling from roll contact and water sprays greatly affects the σ_{yy} (casting direction) stress profile. Surface quenching created surface tension and subsurface compression during water spraying. Both the temperature and stress profiles are symmetric about the strand centerline at this time. At 130s below the meniscus, when the shell was 25 mm thick, water sprays and roll contacts lowered the strand surface temperature from 1265°C to 1167°C and 1220°C respectively. The increased heat extraction from water sprays and roll contact affects the strand temperatures up to ~5 mm below the strand surface. The transient surface cooling causes tension at the strand surface. Because of the rapid increase in surface cooling during water sprays, subsurface compression is experienced 5 mm deep into the steel strand.

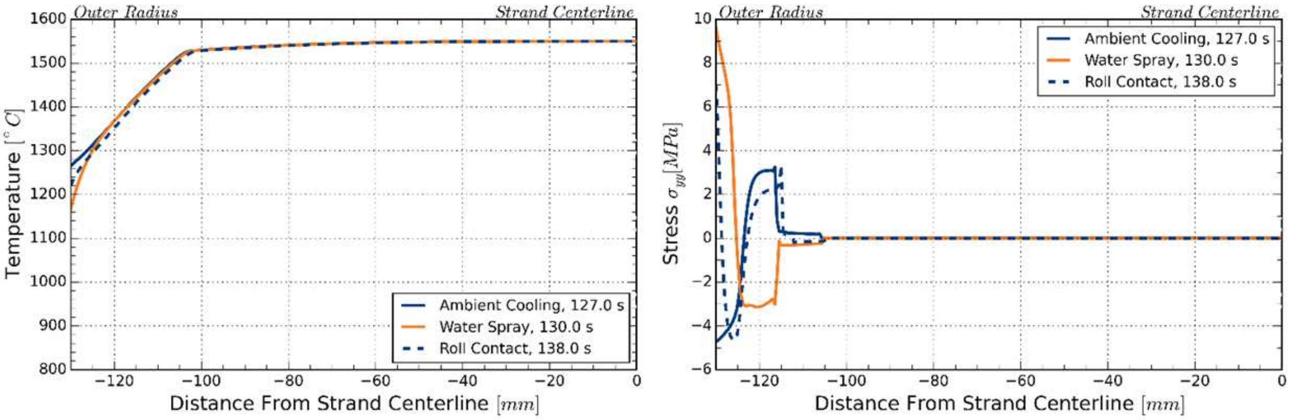

Figure 7. Symmetric temperature and stress profiles through the steel strand before bending was applied.

The temperature and σ_{yy} profiles through the steel strand while bending was applied are shown in Figure 8. The stress profile was asymmetric as bending causes increasing tension closer to the inside-radius and increasing compression closer to the outside-radius. At 180s below the meniscus, when the shell was 30 mm thick, water sprays and roll contacts lowered the strand surface temperature from 1218°C to 1127°C and 1188°C respectively. The rapid temperature changes at the strand surface due to water sprays and roll contact actually caused tension at the both the IR and OR strand surfaces, even while the IR experiences net compression during bending. During roll contact, the OR experienced higher average tension than during ambient cooling or water spray. During water spray cooling, higher subsurface compression was experienced 5 mm below the IR surface than during ambient cooling.

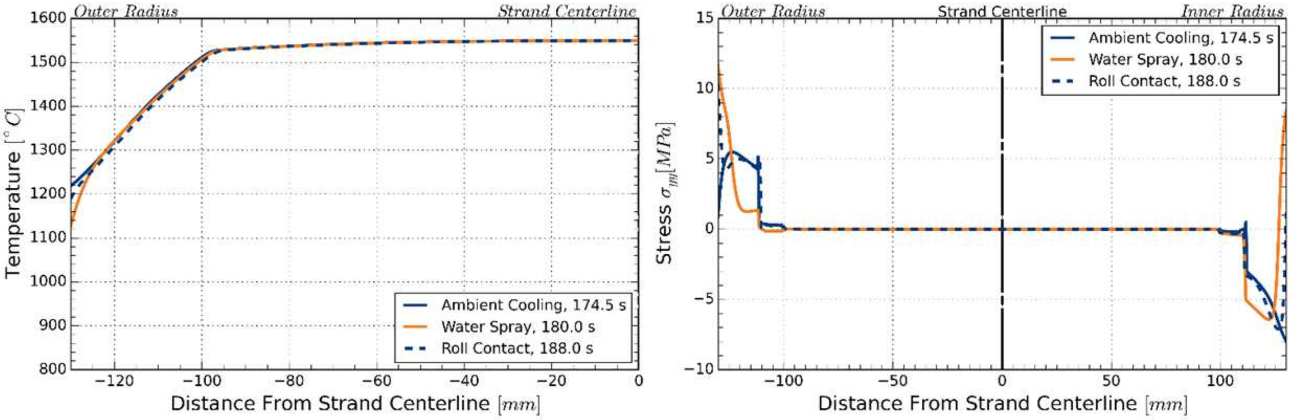

Figure 8. Temperature and stress profiles through the steel strand while bending was applied.

Unbending occurred 1424s below the meniscus when the steel shell was 115 mm thick. The temperature and stress profiles during unbending are shown in Figure 9. Water sprays and roll contact lowered the strand surface temperature from 911°C to 855°C and 883°C, respectively. The strand surface temperatures decreased less from water spray and roll contact during unbending than during bending because the strand surface temperature is lower. Water spray cooling and roll contact only affected the strand temperatures up to 5 mm below the strand surface. The σ_{yy} stresses in the strand at longer times from the meniscus were larger because the solid steel shell was colder and thicker. While unbending was applied, during ambient cooling, net compression was generally experienced at the OR and net tension at the IR. During water spray cooling and roll contact, tension was experienced at the OR surface even though compression was being applied due to unbending.

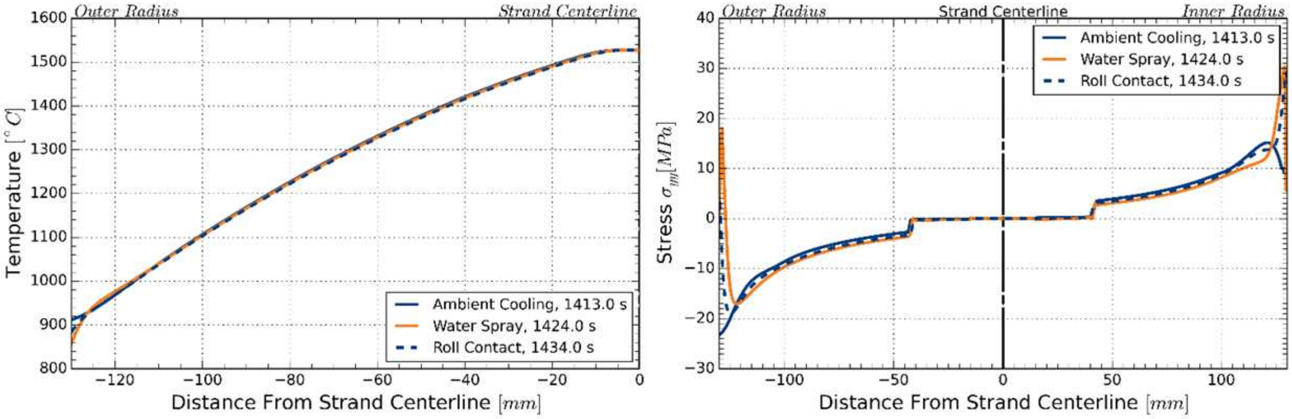

Figure 9. Temperature and stress profiles through the steel strand while unbending was applied.

The effects of non-uniform heat extraction during secondary cooling created cyclic mechanical loading throughout the steel strand. Figure 10 illustrates the mechanical loading the IR strand surface experienced due to the non-uniform heat extraction. Thermal strain was not included in these stress-strain cycles. Before bending occurred, the IR surface experienced stress-strain cycles with small changes in stress but large changes in strain. Water sprays created larger stress-strain cycles than did roll contacts. During bending, when compression was applied, the IR still experienced tensile stresses of ~10 MPa during water spray cooling. A net compressive strain of approximately 1.0% was experienced at the IR surface during bending. When the shell was thicker and colder after unbending, the stresses become larger and the changes in strain become smaller. During unbending the IR surface experienced a net tensile strain of approximately 0.8% and a peak tensile stress of 33 MPa.

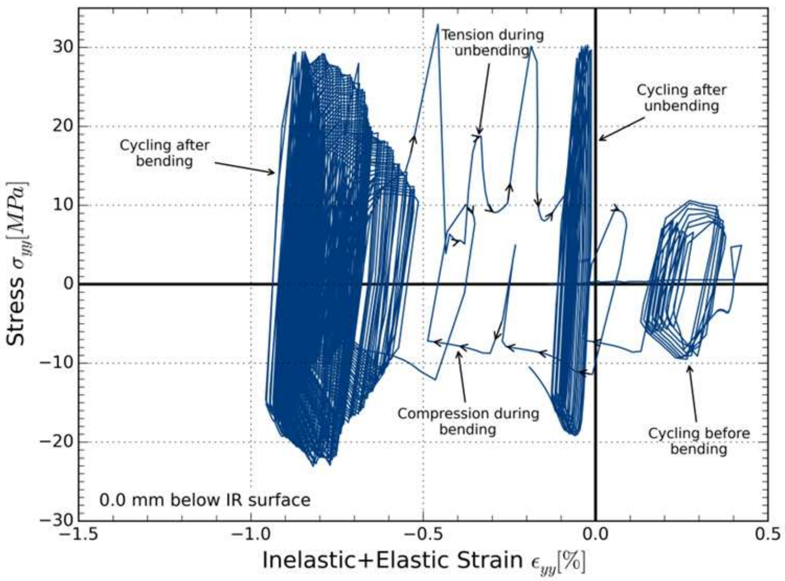

Figure 10. Cyclic loading at the inner radius (IR) surface from meniscus to caster exit.

The mechanical loading experienced at the OR strand surface was very similar to the IR strand surface because the thermal boundary conditions in this model were symmetric. Figure 11 shows the stress-strain loading experienced at the OR surface. The OR experienced cyclic loading similar to the IR, except during bending and unbending. After bending occurred and the OR surface experienced net tension of 0.9%, the OR surface experienced cyclic loading at a net tensile strain. During unbending when net compression was applied at the OR, tensile stress was briefly experienced during water spray cooling and during roll contact. During bending when net tension was applied at the OR, brief compression was experienced at the strand surface. These results show that while bending and unbending apply net tension and compression at the IR and OR, secondary cooling can overcome these effects.

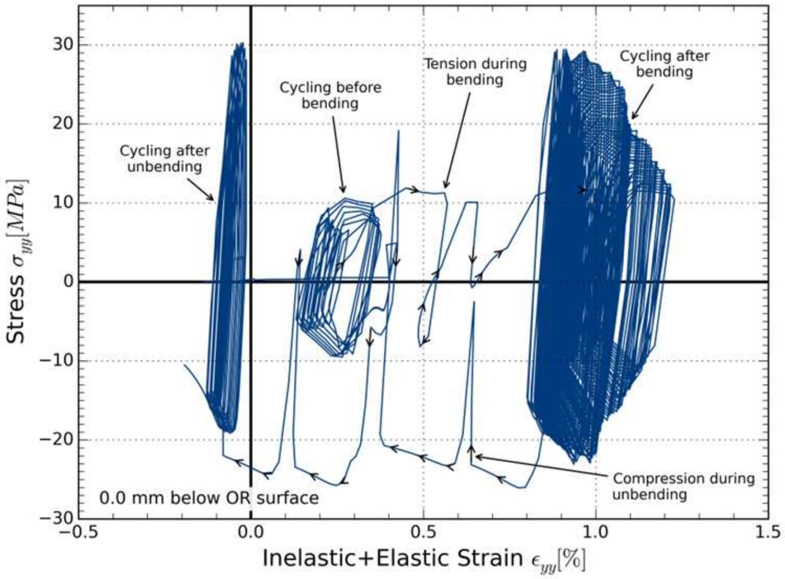

Figure 11. Cyclic loading at the outer radius (OR) surface from meniscus to caster exit.

The total number of stress cycles experienced by the strand is shown in Figure 12. The number of stress cycles increases with time and decreases with distance below the strand surface. The latter trend is relatively linear. The four times when stress cycles are plotted were chosen at equal intervals down the caster. The stress cycling through the strand thickness was symmetric about the strand centerline, again, owing to the symmetric thermal boundary conditions. While the IR and OR experienced different loading during bending and unbending, the heat extraction in secondary cooling dominated the stress-strain cycling behavior. To avoid counting small numerical fluctuations of σ_{yy} as loading cycles, only stress cycles with magnitudes larger than 0.5 MPa were counted.

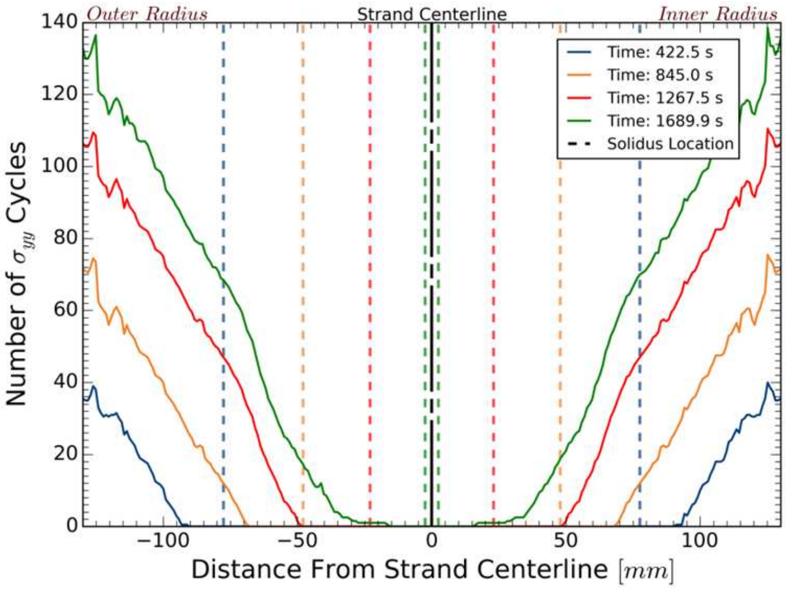

Figure 12. Total number of stress cycles through the strand thickness.

The average magnitude of the stress cycles experienced through the strand decreased very rapidly with distance below the strand surface, as illustrated in Figure 13 at four times. At caster exit, the strand surface had experienced stress cycles with an average magnitude of 34 MPa, but 10 mm below the strand surface the average stress cycle magnitude was 5 MPa. The stress cycle magnitude was also symmetric about the strand centerline because the thermal boundary conditions are symmetric, and surface heat extraction controlled the stress cycling behavior. Only average stress cycle magnitudes larger than 0.5 MPa were included. The average stress cycle magnitude decreased to roughly constant values at depths greater than 25 mm below the strand surface. A rapid decrease in stress cycle magnitude with distance below the strand surface was seen at all four different times.

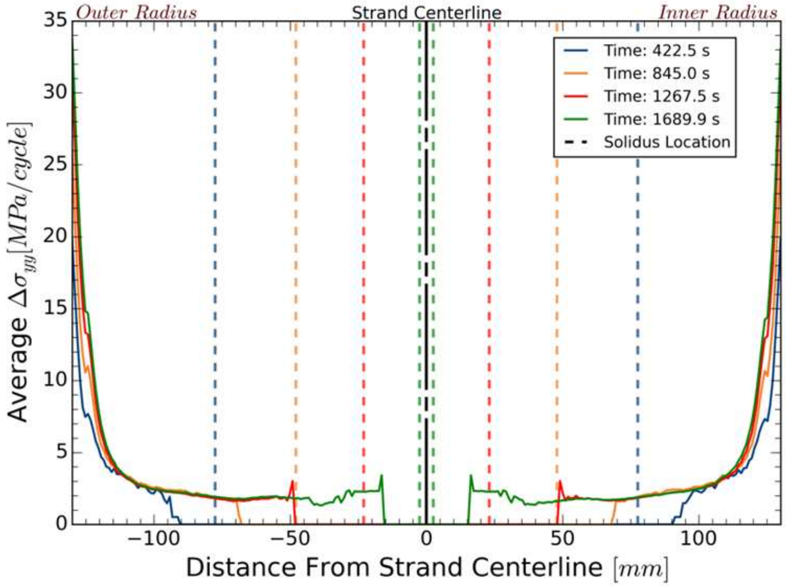

Figure 13. Average magnitude of the stress cycles experienced through the strand thickness.

The stress-strain cycling of the steel strand indicates that high-temperature low-cycle fatigue of the steel strand should be considered in predictions of transverse crack formation. Low-cycle fatigue should be considered by investigating the inelastic strain the material experiences to determine the risk of failure and formation of transverse cracks, according to Coffin and Manson[16]. Figure 14 shows the total number of inelastic strain cycles experienced by the steel strand in the casting direction. The number of inelastic strain cycles experienced by the steel strand is very different than the number of stress cycles experienced. Large stresses are required to cause inelastic strains, and so significant inelastic strain cycling occurs only within the first 5 mm of the strand surface, where large stress cycling occurred. The number of inelastic strain cycles experienced by the strand is symmetric about the strand centerline. To eliminate the effects of small numerical fluctuations, inelastic strain cycles with a magnitude less than 0.05% were not counted. Counting of the inelastic strain and stress cycles was performed using a rain flow algorithm from Amzallag[17].

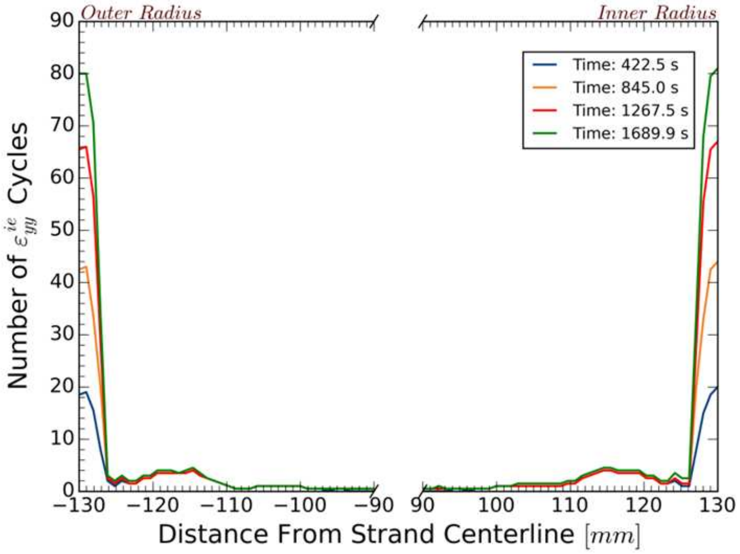

Figure 14. Total number of inelastic strain cycles in first 40 mm below the strand surface.

The total number of inelastic strain cycles gives some insight into the inelastic strain cycling experienced by the steel strand during secondary cooling. The magnitude of the inelastic strain cycles, and the total accumulated inelastic strain, also give important information about the low-cycle fatigue failure of the steel. Figure 15 shows the total accumulated inelastic strain through the steel strand, which was calculated by summing the magnitudes of the inelastic strain in each cycle. The total accumulated inelastic strain through the steel strand is very symmetric about the strand centerline. At caster exit, the strand surface experienced a total of 47% accumulated inelastic strain due to thermal cycling in secondary cooling. The majority of accumulated inelastic strain is within 5 mm of both the IR and OR strand surfaces. At 5 mm below the OR strand surface, less than 3% of inelastic strain has been accumulated.

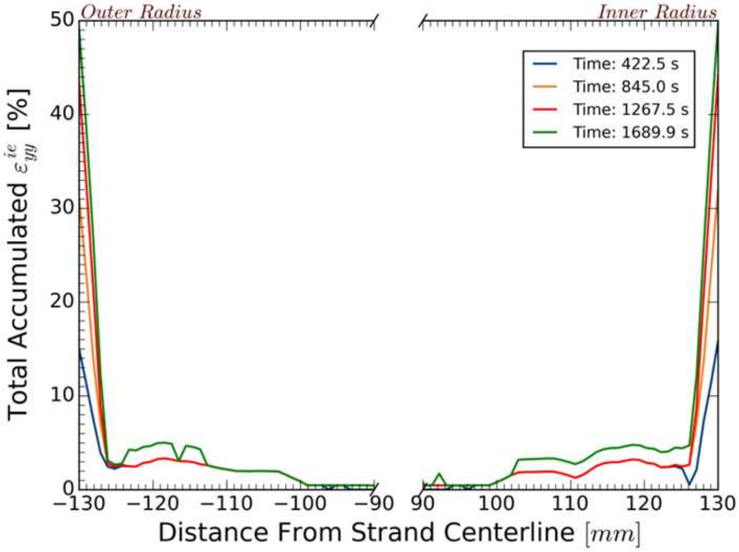

Figure 15. Total accumulated inelastic strain in first 40 mm below the strand surface.

The most severe temperature fluctuations due to water sprays and roll contact in secondary cooling occurred within 5 mm of the strand surface. This caused severe stress-strain cycling within the same region near the surface. This cycling caused large amounts of inelastic strain to accumulate. It is likely that these inelastic strains would contribute to the formation of transverse cracks as characterized by high-temperature low-cycle fatigue. There were no significant differences in the fatigue behavior observed at the IR and OR of the strand, because the thermal boundary conditions at the strand surface were symmetric. The IR surface experienced a tensile strain of 0.8% during unbending and a peak tensile stress of 33 MPa.

CONCLUSIONS

This work presents a simple, efficient thermo-mechanical Lagrangian model of a narrow slice through the center of a typical thick-slab caster. It was applied to investigate the effect of water spray, roll contact, bending, and unbending on the mechanical response of the steel strand as it moves through the entire caster. During cooling due to water sprays or roll contacts, the decreasing thermal strains at the strand surface create large amounts of tension and inelastic strain at the strand surface. Subsequent surface reheating then creates compression again at the strand surface. This alternating temperature history affects temperatures up to 5mm beneath the strand surface, which causes alternating cycles of tension and compression throughout the strand thickness. Because the thermal boundary conditions were the same on IR and OR, the stress-strain cycling at the strand surface was also symmetric. Plant experience, however, shows that transverse crack formation tends to occur at the IR surface during unbending. This suggests that low-cycle fatigue creates transverse cracks, arising from thermal cycling during secondary cooling, combined with mean tension and accumulated tensile inelastic strain experienced at the OR surface during bending and at the IR surface during unbending, and with microstructural changes, such as ferrite networks and precipitates at the austenite grain boundaries.

This new modeling tool to generate the stress and inelastic strain cyclic mechanical loading histories of the steel strand during secondary cooling can be used to design better experiments for quantifying steel ductility. Cyclic loading of steel specimens in Gleeble machines that mimic mechanical loading actually experienced locally in the strand during secondary cooling and unbending will give more quantitative results about the possible risk of transverse crack formation at the surface for a specific steel grade and secondary cooling conditions. New test conditions for steel ductility that account for cyclic loading that occurs in the caster will also give information about how to modify secondary cooling conditions to avoid transverse cracking.

ACKNOWLEDGEMENTS

The authors would like to thank the members of the Continuous Casting Consortium at the University of Illinois Urbana-Champaign for their financial support of this research, and Dr. L.C. Hibbeler for his assistance on this project and report.

REFERENCES

1. Y. Meng and B. G. Thomas, “Heat-transfer and solidification model of continuous slab casting: CON1D,” *Metallurgical and Material Transactions B*, vol. 34, no. 5, pp. 685–705, Oct. 2003.
2. *Abaqus 6.13 Documentation Collection*. Dassault Systemes, 2013.
3. B. Mintz and D. N. Crowther, “Hot ductility of steels and its relationship to the problem of transverse cracking in continuous casting,” *International Materials Reviews*, vol. 55, no. 3, pp. 168–196, May 2010.
4. E. S. Szekeres, “A Review of Strand Casting Factors Affecting Transverse Cracking,” in *Proceedings of the 6th International Conference on Clean Steel*, 2002.
5. T. Kato, Y. Ito, M. Kawamoto, A. Yamanaka, and T. Watanabe, “Prevention of Slab Surface Transverse Cracking by Microstructure Control,” *ISIJ International*, vol. 43, no. 11, pp. 1742–1750, 2003.
6. U. H. Lee, T. E. Park, K. S. Son, M. S. Kang, Y. M. Won, C. H. Yim, S. K. Lee, I. Kim, and D. Kim, “Assessment of Hot Ductility with Various Thermal Histories as an Alternative Method of *in situ* Solidification,” *ISIJ International*, vol. 50, no. 4, pp. 540–545, 2010.
7. M. El-Wazri, F. Hassani, S. Yue, E. Es-Sadiqi, L. E. Collins, and K. Iqbal, “The Effect of Thermal History on the Hot Ductility of Microalloyed Steels,” *ISIJ International*, vol. 39, no. 3, pp. 253–262, 1999.
8. Santillana, L. C. Hibbeler, B. G. Thomas, A. Hamoen, A. Kamperman, and W. V. D. Knoop, “Heat Transfer in Funnel-mould Casting: Effect of Plate Thickness,” *ISIJ International*, vol. 48, no. 10, pp. 1380–1388, 2008.
9. S. Koric and B. G. Thomas, “Efficient thermo-mechanical model for solidification processes,” *Int. J. Numer. Meth. Engng.*, vol. 66, no. 12, pp. 1955–1989, Jun. 2006.
10. L. Yu, “FEM analysis of bulging between rolls in continuous casting,” M.S., University of Illinois at Urbana-Champaign, United States -- Illinois, 2000.
11. V. D. Fachinotti and A. Cardona, “A fixed-mesh Eulerian–Lagrangian approach for stress analysis in continuous casting,” *Int. J. Numer. Meth. Engng.*, vol. 70, no. 6, pp. 728–755, May 2007.
12. P. F. Kozlowski, B. G. Thomas, J. A. Azzi, and H. Wang, “Simple constitutive equations for steel at high temperature,” *Metallurgical and Materials Transactions A*, vol. 23, no. 3, pp. 903–918, Mar. 1992.
13. H. Zhu, “Coupled thermal-mechanical fixed-grid finite-element model with application to initial solidification,” Ph.D., University of Illinois at Urbana-Champaign, United States -- Illinois, 1997.
14. T. Nozaki, J. Matsuno, K. Murata, H. Ooi, and M. Kodama, “SECONDARY COOLING PATTERN FOR PREVENTING SURFACE CRACKS OF CONTINUOUS CASTING SLAB.,” vol. 18, no. 6, pp. 330–338, 1978.
15. B. Petrus, D. Harnmon, M. Miller, B. Williams, A. Zewe, Z. Chen, J. Bentsman, and B. G. Thomas, “New method to measure metallurgical length and application to improve computational models,” in *AISTech 2015 Iron and Steel Technology Conference and 7th International Conference on the Science and Technology of Ironmaking, ICSTI 2015*, 2015, vol. 3, pp. 3238–3248.
16. L.F. Coffin, “Low-cycle fatigue,” *Metals Engineering Quarterly*, vol. 3, no. 4, pp. 15–24, 1963.
17. C. Amzallag, J. P. Gerey, J. L. Robert, and J. Bahuaud, “Standardization of the rainflow counting method for fatigue analysis,” *International Journal of Fatigue*, vol. 16, no. 4, pp. 287–293, Jun. 1994.